UNITED STATES DEPARTMENT OF THE INTERIOR

GEOLOGICAL SURVEY

A DESCRIPTION OF COLORED GRAVITY AND TERRAIN MAPS FOR THE UNITED STATES AND ADJACENT CANADA EAST OF 104°

by

R. W. Simpson, T. G. Hildenbrand , R. H. Godson, and M. F. Kane

Open-File Report 82-877

1982

A Description of Colored Gravity and Terrain Maps

for the United States and Adjacent Canada East of 104°

by

R. W. Simpson, T.G. Hildenbrand, R.H. Godson, and M.F. Kane

INTRODUCTION

Using an Applican Color Plotter, we have plotted the gravity and terrain data available to us for the portion of the United States east of 104° longitude and adjacent parts of Canada. Standard 2"x2" color slides of these maps are available through the U.S. Geological Survey Photo Library (Mail Stop 914, Box 25046, Denver Federal Center, Denver, CO, 80225, telephone 303/234-4004).

These maps were originally prepared for studies in the Earthquake Hazards and Reactor Hazards Programs to examine possible spatial correlations of seismicity with features in the gravity field. It appears that in many cases, earthquakes in the eastern United States occur in proximity to ancient structures which are marked by gravity gradients. This is consistent with the world-wide correlations of intraplate seismicity and pre-existing zones of weakness documented by Sykes (1978).

THE DATA SETS

1. Gravity Data

The gravity data were extracted from the Department of Defense (DOD) gravity data file available through the National Oceanic and Atmospheric Administration (NOAA) Data Center. (NOAA, National Geophysical and Solar Terrestrial Data Center, Boulder, CO 80302). Canadian gravity data were obtained from the Canadian Gravity Data Centre (1 Observatory Crescent, Ottawa, Canada K1A 0Y3). Additional data from the Coastal Plain of South Carolina collected by Alan Cogsbill were supplied by the Geothermal Program at Virginia Polytechnic Institute.

The basic data set was screened to extract at most one station for every 4 km x 4 km cell in order to obtain a more uniform density of data points. Not surprisingly, some bad values have crept into the data set, and these are especially apparent in the gradient and derivative maps where they show up as small four-petal flower patterns. Questions about single small anomalies should always be referred to larger scale maps and to the original published maps whenever possible. We are confident that the major anomalies and trends are real, and there is excellent correspondence of many smaller anomalies with mapped geologic units.

A minimum curvature algorithm (Briggs, 1974) programmed by Webring (1981), was used to do the necessary interpolation and extrapolation to produce a rectangular grid of values with 4.064 km interval between grid points. This interval was chosen so as to be compatible with the pixel size

required by the Applicon Color Plotter. White areas on the maps indicate that there were no data points within 8 km of the grid point.

The data were projected using the Albers Conic Equal-Area projection with standard parallels for the U.S. (29.5°N, 45.5°N), so that the maps are compatible in projection with the U.S. Geologic Map (King and Beikman, 1974).

2. Terrain Data

Terrain data were obtained from the National Geodetic Survey (NGS) who in turn received it from the Electromagnetic Compatability Analysis Center (ECAC), an agency of the Department of Defense (DOD). The data were extensively edited and reformatted (by R. H. Godson) to produce average elevations for the entire country at 30", 1', and 3' intervals. This data set has been submitted to the NOAA Data Center (National Geophysical and Solar-Terrestrial Data Center, National Oceanic and Atmospheric Administration, Boulder, CO 80303) for distribution.

DESCRIPTION OF THE MAPS

1. Station Locations

This map shows the location of the 132,217 screened gravity stations used.

2. Free Air Gravity

This map displays the free air anomaly field calculated using the 1967 Geodetic Reference System formula for theoretical gravity (International Association of Geodesy, 1971). Observed gravity values have been adjusted to conform to the International Gravity Standardization Net of 1971 (Morelli, 1974). The free air values for the set of screened gravity stations were gridded directly to produce this map. A better technique to avoid sample bias (Garland, 1980) might be to calculate a free air gravity field from the Bouguer gravity and the terrain. Values on the color scales are listed in Appendix A.

3. Bouguer Gravity

Bouguer anomalies were also calculated using the new geodetic reference system (see references above) and a reduction density of 2.67 g/cm^3. Except for the flatter areas in the mid-continent, land stations in the U.S. have been computer terrain corrected into a distance of 0.895 km from the station using a program of Plouff (1977). Estimated error in the Bouguer gravity values on most land stations is less than about 2 milligals. Marine stations and lake stations may sometimes be in error by as much as 10 milligals.

4. Bouguer 250 km Lopass

Using a Fourier transform filtering program written by Hildenbrand (1979), wavelengths shorter than 250 km in the Bouguer anomaly field were suppressed. (A "lopass" filter with a linear ramp between 200 km and 300 km was used in the wave number domain.) The result is a smooth regional gravity

field which contains much of the effects of the isostatic roots under high topography. It is these roots that give the Bouguer map such a strong negative correlation with topography.

5. Bouguer 250 km Hipass

This map was obtained by subtracting the 250 km Lopass data from the Bouguer data, a process equivalent to using a wavelength filter which passes only wavelengths shorter than 250 km. As before, the cutoff is actually a ramp from 200 km to 300 km. Thus the Hipass map and the Lopass map "add up" to the Bouguer map.

Examples of the wavelength filtering process are discussed in Appendix B. Ulrych (1968) has pointed out that the short wavelength component of filtered gravity highs will acquire flanking lows of lesser magnitude on either side. This tends to give the whole map a grain roughly equal in wavelength to the cut of the filter. Thus all anomalies must be interpreted with care. The dangers, we feel, are more than compensated for by the enhancement of many structures, trends, and features of geologic interest.

6. Bouguer 125 km Lopass

Again wavelength filtering was applied to the Bouguer anomaly map to produce a regional gravity map consisting of wavelengths longer than 125 km. (A "lopass" filter was used with a linear ramp from 100 km to 150 km.)

7. Bouguer 125 km Hipass

This map was derived by subtracting the 125 km Lopass map from the original Bouguer anomaly map. The result is equivalent to a residual map consisting of wavelengths shorter than 125 km obtained by using a "hipass" wavelength filter. The same cautions apply as for the 250 km Hipass map--anomalies will tend to be flanked by smaller amplitude anomalies of opposite polarity. A 125 km anomaly grain produced by the wavelength filtering is quite obvious in this map. The reality of features of interest can often be verified by examining the second vertical derivative which is a much smoother form of high pass filtering which does not introduce an anomaly grain at the cutoff wavelength. For modeling purposes, the original Bouguer data should be consulted.

The anomalies which are displayed in this map correspond to crustal source bodies. The tests described in Appendix B indicate that sources deeper than 40 km are almost entirely removed by hipass filtering at 125 km, and that sources at depths greater than 20 km are severely attenuated.

Note, however, that not all the anomalies produced by near-surface sources have escaped the filtering; broader anomalies produced by facies changes or the gradual feathering of density contrasts over distances greater than 125 km will also be surpressed, even though the density contrast may be very near the surface.

8. Second Vertical Derivative of Bouguer Anomalies

The second vertical derivative of the Bouguer anomaly field was calculated

using Hildenbrand's Fourier transform filtering program. The effect of this filter is to multiply the various wavelength components of the Bouguer Field by $(1/\text{wavelength})^2$, which greatly enhances the shorter wavelengths and, hence, the near-surface density contrasts. The zero level of the second vertical derivative marks the steepest portions of linear anomalies, and is frequently taken as a good indicator of the position of density contrasts and the horizontal extent of geologic bodies. This map, of all the maps, is most likely to exhibit anomalies which correlate with mapped bodies and features exposed at the surface.

Because this filter greatly enhances the short wavelengths--including those associated with bad data points--the data were initially upward continued to an elevation of 10 km before applying the second derivative filter in order to smooth some of the irregularities in the data. This is a compromise between noise and resolution.

9. Horizontal Gradient of the Bouguer Gravity

The magnitude of the horizontal gradient of the Bouguer anomaly field was calculated using the basic equation:

$$\left|\text{gradient}\right| = \sqrt{\left(\frac{\partial z}{\partial x}\right)^2 + \left(\frac{\partial z}{\partial y}\right)^2}$$

and the approximations that

$$\left(\frac{\partial z}{\partial x}\right)_{i,j} = \frac{z_{i+1,j} - z_{i-1,j}}{2(\Delta x)}, \text{ and } \left(\frac{\partial z}{\partial y}\right)_{i,j} = \frac{z_{i,j+1} - z_{i,j-1}}{2(\Delta y)}$$

This approximation can be shown to be equivalent to fitting a parabola at grid point i using z_i and its 2 neighboring values z_{i+1}, z_{i-1} and then calculating the slope of the parabola at i. The magnitude of the gradient of an anomaly depends on both the size of the density contrast and the nearness of the source to the surface. The largest gradients will often occur nearly over the mass contrast at the edges of geologic bodies. Cordell (1979) developed the horizontal gradient method to locate faults.

Horizontal gradients produced by linear anomalies are steepest over the two sides and gentle or flat along the tops of the anomalies so that there are two flanking high gradients (red) and a medial low gradient (blue). Nearly circular anomalies have their highest gradients going around them. The result on the color map is a red doughnut encircling the anomaly. Many linear gradients are thought to mark major faults and structural boundaries of plate tectonic significance. Circular gradients outline, in many cases, felsic and mafic plutonic bodies.

McGinnis and Ervin (1974), Long (1976), Forsyth (1977), and Simmons and others (1978) have pointed out apparent correlations of earthquakes with the gradient of the Bouguer gravity field. Although many earthquakes lie in areas with high gradients, there are also many large gradients which do not show signs of seismicity (compare Hadley and Devine, 1974).

Perhaps the gradients with little associated seismicity mark structures which are not being reactivated since they are not favorably oriented with respect to the regional stress field. Another possibility is that the earthquake record is not long enough to establish the true long-term patterns of seismicity.

It does appear that some areas with low gravity gradients have relatively fewer earthquakes. This may reflect a smaller number of major structures in these areas, but it is also possible that the lower gradients reflect a greater depth to the Precambrian basement which contains the structures under a thick cover of Paleozoic sedimentary rocks. If the Precambrian basement is deeper, it may be in a rheological regime where creep or plastic deformation is more likely to occur than brittle, earthquake-producing fracture.

10. Terrain

The elevation data at 3' intervals were used to prepare this grid. The data were projected (Albers) and regridded to 4.064 km interval to produce a map at a scale of 1:5,000,000 on the color plotter.

APPENDIX A

Color Scale of Slides

1.	Station Locations:	(scale not applicable)
2.	Free Air:	-60 to +55 in steps of 5 milligals
3.	Bouguer Gravity:	-140 to +50 in steps of 10 milligals
4.	250 km Lopass:	-140 to +50 in steps of 10 milligals
5.	250 km Hipass:	-35 to +30 in steps of 5 milligals
6.	125 km Lopass:	-140 to +50 in steps of 10 milligals
7.	125 km Hipass:	-30 to +16 in steps of 2 milligals
8.	2nd Vertical Derivative:	-.16 to +.16 in steps of .02 milligals/km^2
9.	Horizontal Gradient:	0 to 2.5 in steps of 0.1 milligals/km
10.	Terrain:	1 to 1033 in steps of 33 meters

APPENDIX B

Tests of Wavelength Filtering

In order to examine the shapes of the regionals and residuals produced by wavelength filtering and to test the relationship between wavelength cut and depth of source, we filtered the anomalies produced by some simple source bodies. The resulting anomalies, displayed in this appendix, are plotted in profile rather than in map view. Additional examples of wavelength filtering applied to potential field data and discussions of the limitations are to be found in Zurflueh (1967) and Ulyrch (1968).

Figure 1 exhibits the effects of wavelength filtering using different cutoff wavelengths as applied to the gravity anomaly produced by an infinitely long horizontal cylinder at 10 km depth. The mass of the cylinder has been adjusted to produce an anomaly with 1 milligal peak amplitude. The anomaly was sampled at 1 km intervals from -100 km to +100 km. The profile was extended from 201 points to 512 points to eliminate edge effects and speed the Fourier transform (Cordell and Grauch, 1982). The extension used was a simple linear trend from the value at one end of the profile to that found at the other end, so that no discontinuities in value exist when the ends of the profile are "joined" by the finite Fourier transform. The wavelength filters were tapered by 20% to either side of the cutoff wavelength. For example, the 250 km cutoff is actually a ramp in the wave number domain running from $(2\pi/200)$ km^{-1} to $(2\pi/300)$ km^{-1}.

Note that at 250 km (Figure 1a) the short wavelength component has not changed in shape much, though it has begun to acquire lows on either side. At 125 km, the shape of the central part of the anomaly is still well preserved, but the lows on either side are starting to become large compared to the amplitude of the anomaly. At 62.5 km neither the short wavelength nor the long wavelength components really fit the original anomaly very well. At 31.25 km, the long wavelength component matches the original anomaly pretty well, though it still cannot fit the high curvature parts of the anomaly. The short wavelength component is becoming quite small.

These results can be scaled according to the depth of the source: for example, if depth is 1 km, similar assertions hold for wavelength cuts which are 1/10 of the values used in Figure 1.

Another way of looking at the interchange of wavelength-cut and depth is shown in Figure 2. Here five horizontal cylinders are used at depths of 1, 5, 10, 20, and 40 kilometers (Figure 2a).

Figure 2b shows the gravity anomalies for these five cylinders normalized so that they all have peak values of 1 milligal.

Figure 2c shows that for a wavelength cut at 250 km, the anomalies of cylinders at 1, 5, and 10 km are not much affected by hipass filtering since they have much of their energy in short wavelengths whereas the anomalies from cylinders at 20 and 40 km have begun to be severely attenuated. Figure 2d shows the long wavelength (lopass) components.

At a wavelength cut of 125 km, the anomaly for the cylinder at 40 km depth has been almost completely removed in the short wavelength (hipass) component and is almost entirely contained in the long wavelength (lopass) component.

In summary, at 125 km wavelength cut, linear anomalies produced by cylinder like sources lying at depths greater than 40 km will be largely removed from the short wavelength (hipass) residual, but will remain essentially unchanged in the long wavelength (lopass) regional. Conversely cylindrical sources at depths less than 5 kilometers will be kept essentially unchanged in the short wavelength (hipass) portion. Cylindrical sources with depths in the 10 km to 20 km range will have significant contributions in both long and short wavelength components.

Thus wavelength filtering will work best at separating anomalies from sources at different depths if there are distinct families of sources at two different depths, say above 10 kilometers and below 40 kilometers. The depth dependence, however, is further complicated by the existence of horizontally distributed sources, such as the feathering edge of sedimentary basins, which can result in far more long wavelength energy than if the source were more compact (e.g., cylinder like). The isostatic roots which provide compensation for topographic loads at the earth's surface are of such a nature and it is to a large degree the effects of these roots which have been removed in the 250 km Hipass (short-wavelength) map.

Another important factor which has not been considered is the normal fall off in amplitude of anomalies as sources become deeper (Figure 2a). For two dimensional sources--for example, the horizontal cylinder considered above--the amplitude is inversely proportional to the depth. For three dimensional sources--for example, a sphere--the decrease in amplitude goes as $1/d^2$ where d is depth. Thus the anomalies of all but the largest sources are severely damped by depth. We suspect that this helps in many cases to give a cleaner separation of anomalies produced by sources at different depths than our simple examples of wavelength filtering might indicate. In general, however, the ability of wavelength filtering to separate sources by depth will depend on the geometry of the sources and can be properly evaluated only with the help of models.

As a start in this direction, a real example--the midcontinent gravity high--has been tested. This anomaly is thought to be produced by dense intrusive rocks flanked by low density sediments associated with a failed Precambrian rift (King and Zietz, 1971; Chase and Gilmer, 1973). The profile used is from King and Zietz (1971). The original profile is shown in Figure 3a. A digitized version (7 km between points) is shown in Figure 3b, together with the 250 km filtered components. The anomaly is well defined by wavelengths shorter than 250 km and the long wavelength component mostly serves to take out a -60 milligal offset in base level. At 125 km (Figure 3c) the long wavelength and short wavelength components have amplitudes of similar size, and the short wavelength portion is starting to be a poor representation of the anomaly as a whole. At 61.5 km (Figure 3d), the anomaly is very well described by wavelengths longer than 61.5 km except for the steepest parts of the gradients. Thus, except for a shift in datum level ("infinite" wavelength), the anomaly is pretty well fitted by wavelengths in the band between 250 km and 62.5 km.

The source of the anomaly as modeled by King and Zietz (1971) is entirely above 10 kilometers. Another interpretation would be to put a compensating low density root at the Moho to support the high density material (Chase and Gilmer, 1973). This root would help to explain the flanking lows on either side of the anomaly so that they might not need to be explained entirely in terms of near surface, low density sediments. In terms of wavelength filtering, the midcontinent anomaly is of interest because it is produced by density contrasts, some of which have a rather large horizontal extent. This adds considerably to the amount of energy in the long wavelength part of the spectrum compared to the simpler cylinder models discussed before. This may, in fact, be a rather common characteristic of many geologic bodies producing gravity anomalies.

REFERENCES CITED

Briggs, I. C., 1974, Machine contouring using minimum curvature: Geophysics, v. 39, p. 39-48.

Chase, C. G., and Gilmer, T. H., 1973, Precambrian plate tectonics: the midcontinent gravity high: Earth and Planetary Science Letters, v. 21, p. 70-78.

Cordell, Lindrith, 1979, Gravimetric expression of graben faulting in Santa Fe Country and the Espanola Basin, New Mexico: New Mexico Geol. Soc. Guidebook, 30th Field Conf., Santa Fe Country, p. 59-64.

Cordell, Lindrith, and Grauch, V. J. S., 1982, Reconciliation of the discrete and integral Fourier transforms: Geophysics, v. 47, p. 237-243.

Forsyth, D. A., 1977, Relationships between seismicity, free air gravity, and structure in Arctic and eastern Canada (abs.): Earthquake Notes, v. 48, p. 15.

Garland, G. D., 1980, Comment on "Regional free air gravity anomalies and tectonic observations in the United States" by L. D. McGinnis, M. G. Wolf, J. J. Kohsmann, and C. Patrick Ervin: Journal of Geophysical Research, v. 85, p. 4881.

Hadley, J. B., and Devine, J. F., 1974, Seismotectonic map of the United States: U.S. Geological Survey map MF-620, 3 sheets + 8 p.

Hildenbrand, T. G., 1979, Preliminary documentation of program FFTFIL: U.S. Geological Survey, unpublished documentation.

International Association of Geodesy, 1971, Geodetic Reference System 1967: International Association of Geodesy Special Publication, no. 3, 116 p.

King, E. R., and Zietz, Isidore, 1971, Aeromagnetic study of the midcontinent gravity high of central United States: Geological Society of America Bulletin, v. 82, p. 2187-2208.

King, P. B., and Beikman, H. M., compilers, 1974, Geologic map of the United States (exclusive of Alaska and Hawaii): U.S. Geological Survey, 3 sheets, scale 1:2,500,000.

Long, L. T., 1976, Speculations concerning Southeastern earthquakes, mafic intrusions, gravity anomalies, and stress amplification: Earthquake Notes, v. 47, p. 29-35.

McGinnis, L. D., and Ervin, C. P., 1974, Earthquakes and block tectonics in the Illinois Basin: Geology, v. 2, p. 517-519.

Morelli, C., (ed.), 1974, The International Gravity Standardization Net 1971: International Association of Geodesy Special Publication, no. 4, 194 p.

Plouff, D., 1977, Preliminary documentation for a FORTRAN program to compute gravity terrain corrections based on topography digitized on a geographic grid: U.S. Geological Survey Open-File Report 77-534, 45 p.

Simmons, G., Tillson, D., Murphy, V., LeBlanc, G., Doherty, J., Sharp, J., and Roeloff, E., 1978, Gravity, stress, and earthquakes in Washington State and surrounding areas (abs.): 3rd International Conference on Basement Tectonics, 15-19 May 1978, Fort Lewis College, Durango, CO.

Sykes, L. R., 1978, Intraplate seismicity, reactivation of preexisting zones of weakness, alkaline magmatism, and other tectonism postdating continental fragmentation: Reviews of Geophysics and Space Physics, v. 16, p. 621.

Ulyrch, T. J., 1968, Effect of wavelength filtering on the shape of the residual anomaly: Geophysics, v. 33, p. 1015-1018.

Webring, Michael, 1981, MINC: a gridding program based on minimum curvature: U.S. Geological Survey Open-File Report 81-1224, 41 p.

Zurflueh, E. G., 1967, Applications of two-dimensional linear wavelength filtering: Geophysics, v. 32, p. 1015-1035.

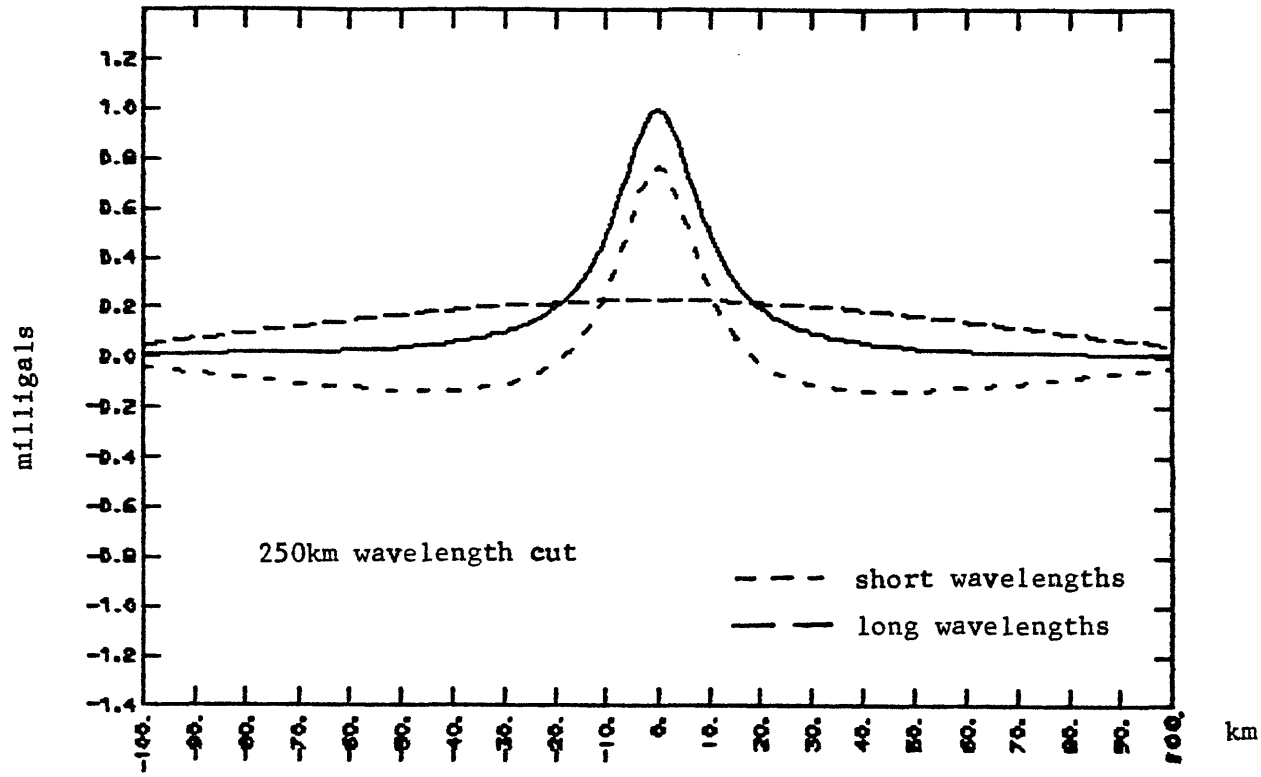

Figure 1a. Gravity anomaly of horizontal cylinder at 10 km depth, wavelength filtered at 250 km. Solid line is vertical force of gravity, short dashes mark short wavelength component, long dashes mark long wavelength component.

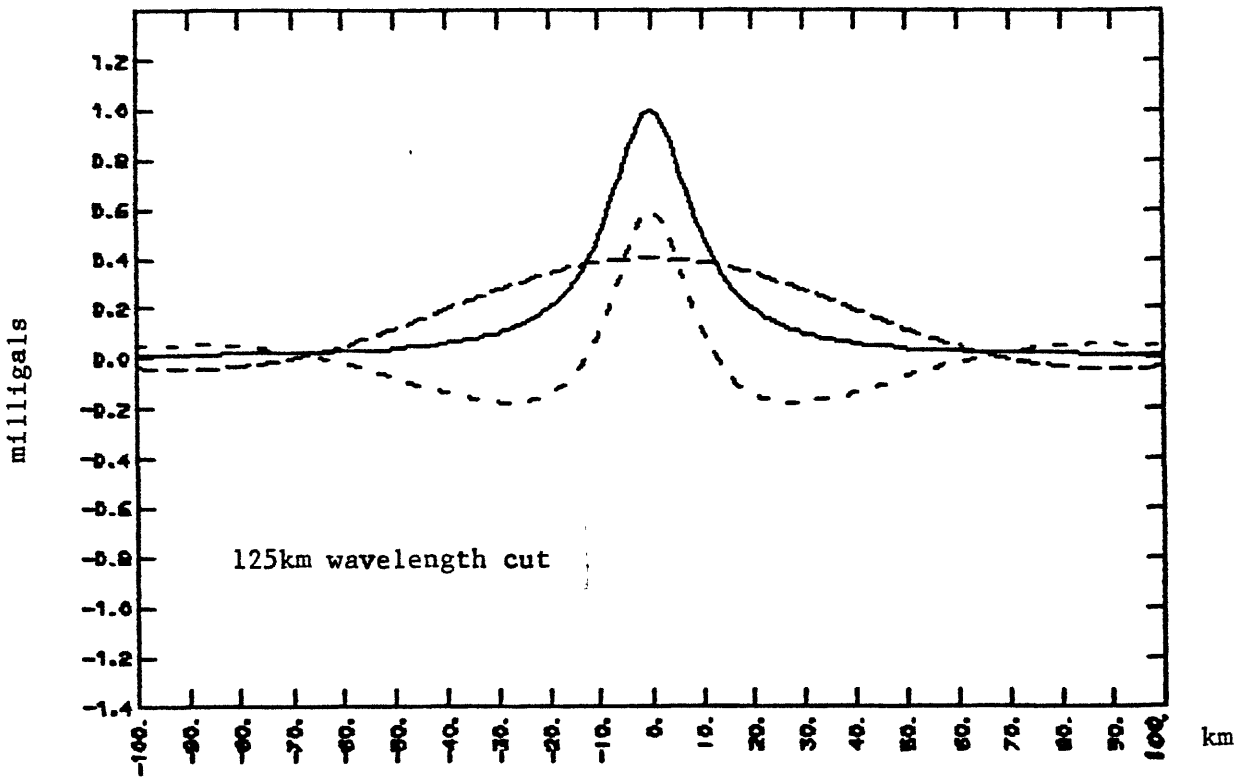

Figure 1b. Same as Figure 1a, but wavelength filter cut at 125 km.

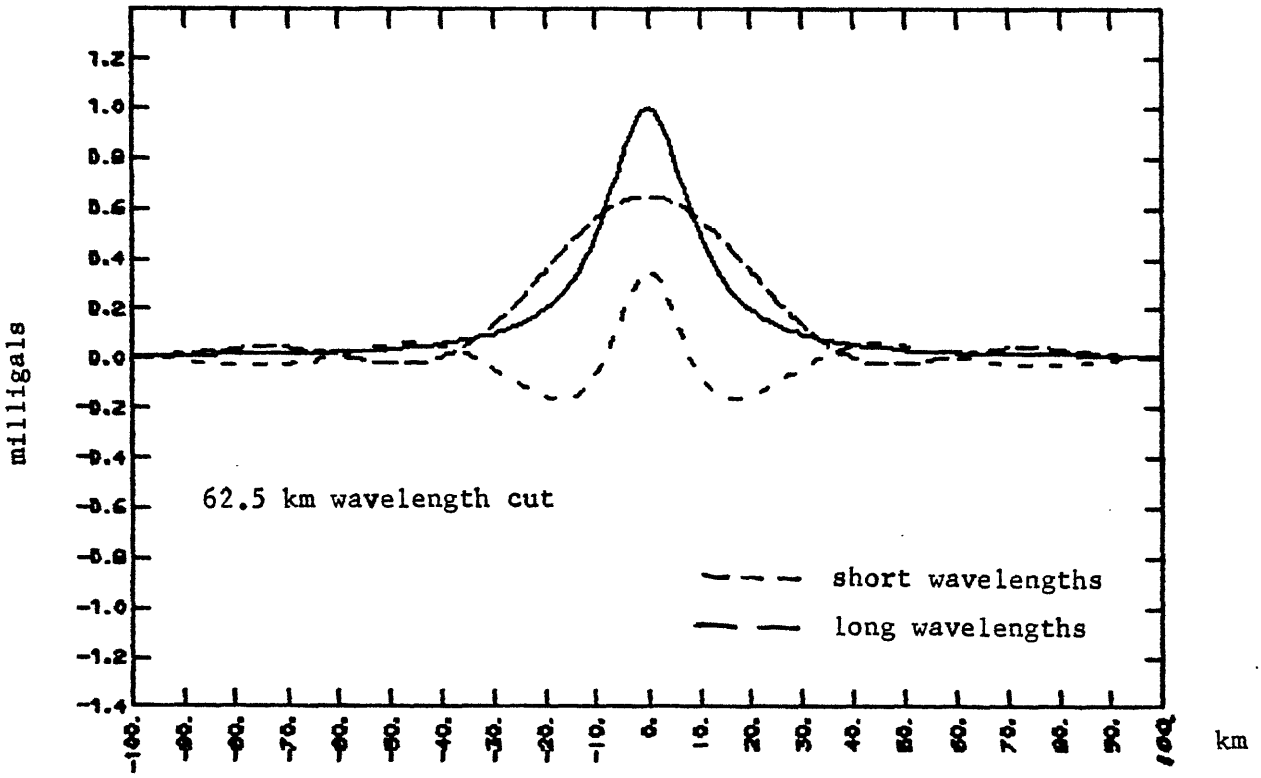

Figure 1c. Same as Figure 1a, but wavelength filter cut at 62.5 km.

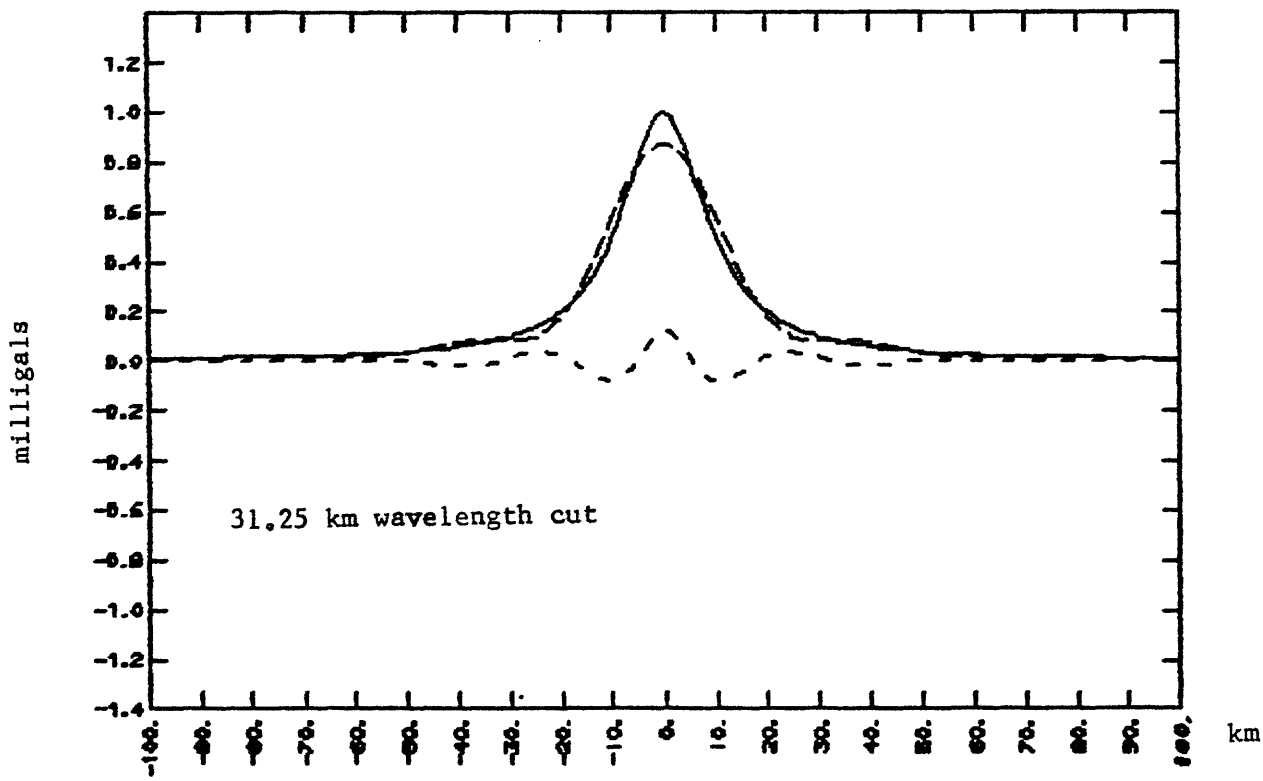

Figure 1d. Same as Figure 1a, but wavelength filter cut at 31.25 km.

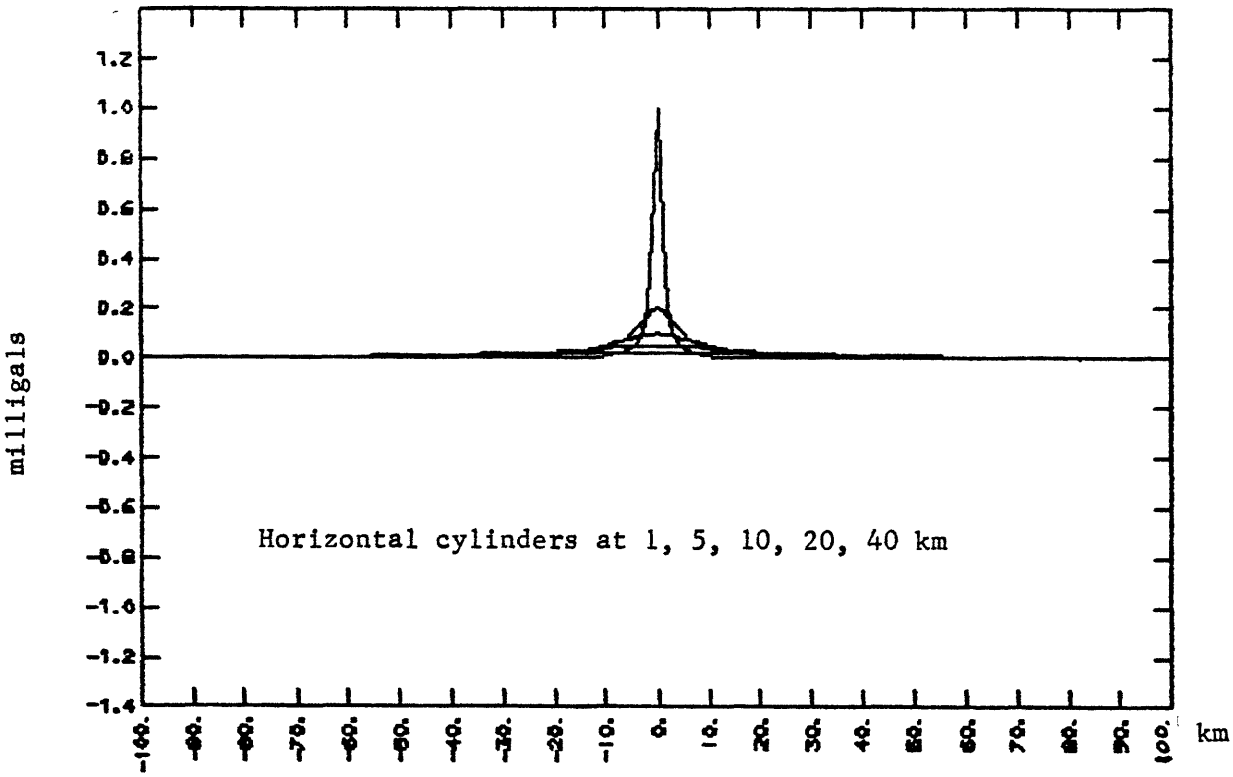

Figure 2a. Vertical force of gravity from horizontal cylinders at depths of 1, 5, 10, 20, and 40 km. Peak amplitude is inversely proportional to depth.

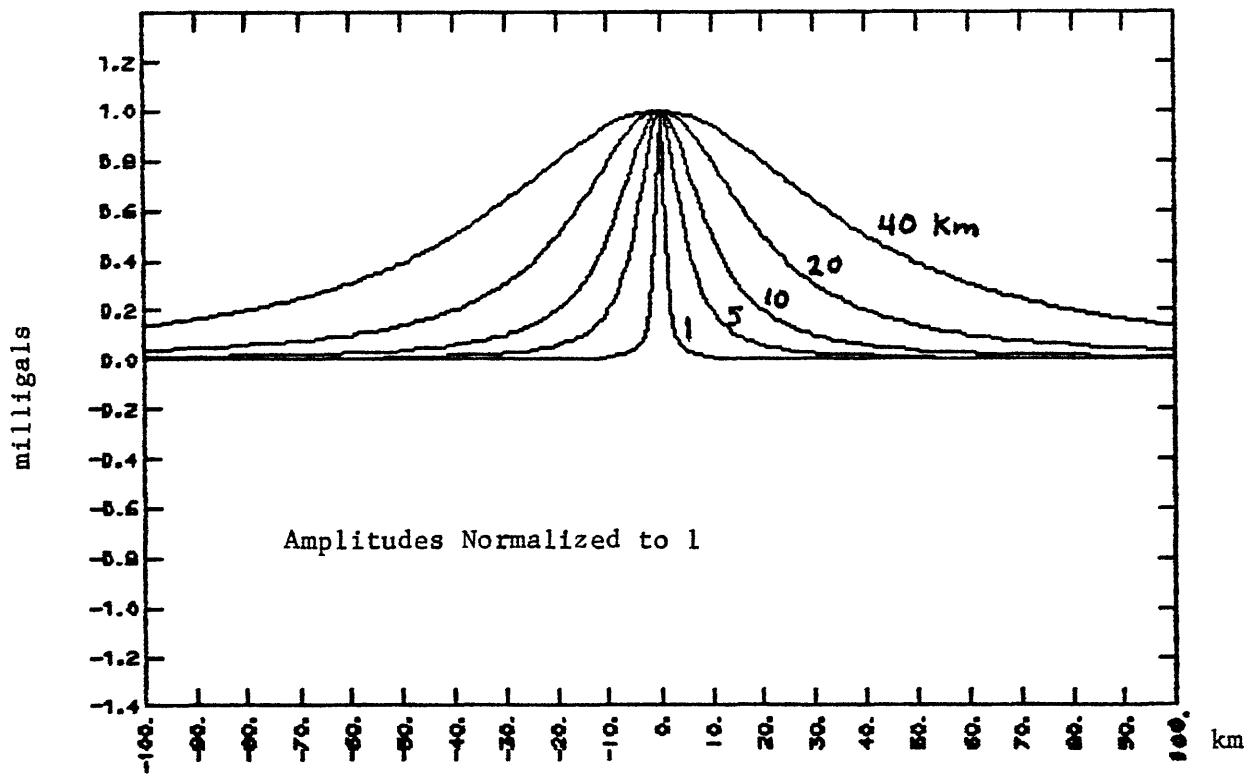

Figure 2b. Same as in Figure 2a, except that peak amplitude of the anomalies has been normalized to 1 milligal.

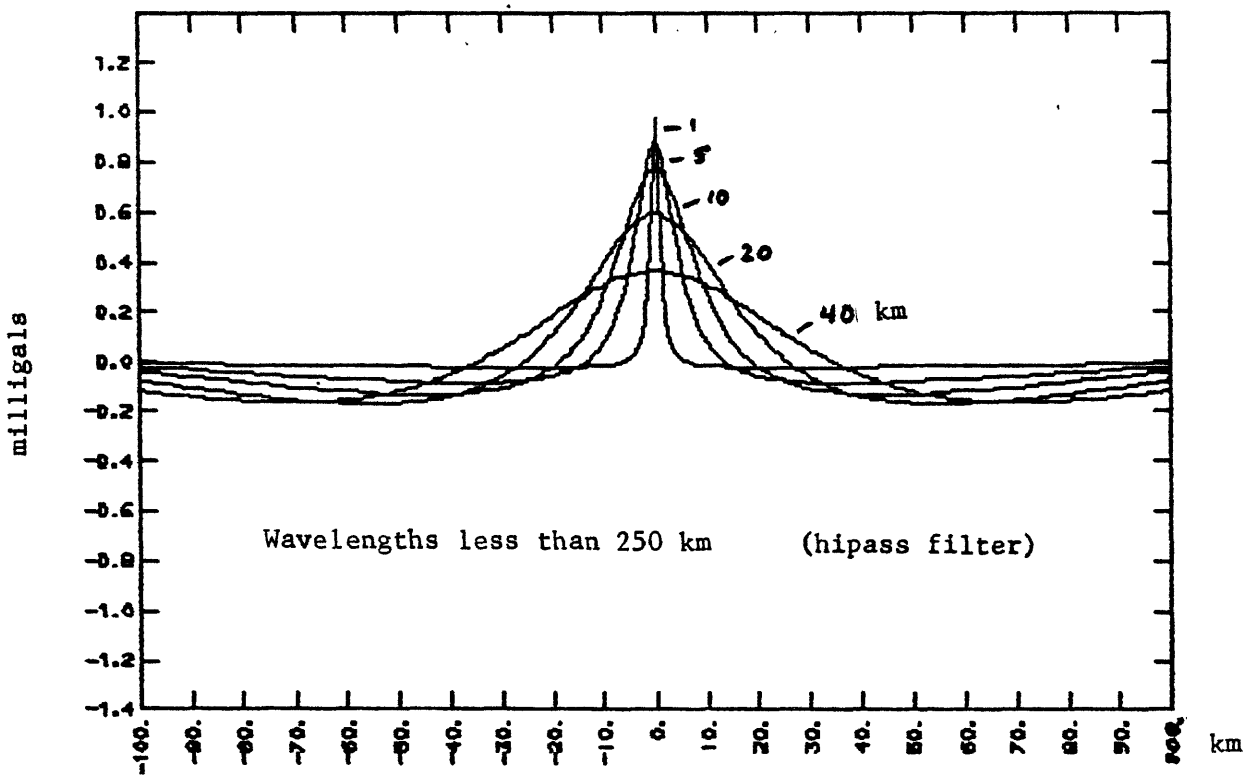

Figure 2c. Short wavelength component (less than 250 km) for same bodies as in figure 2b.

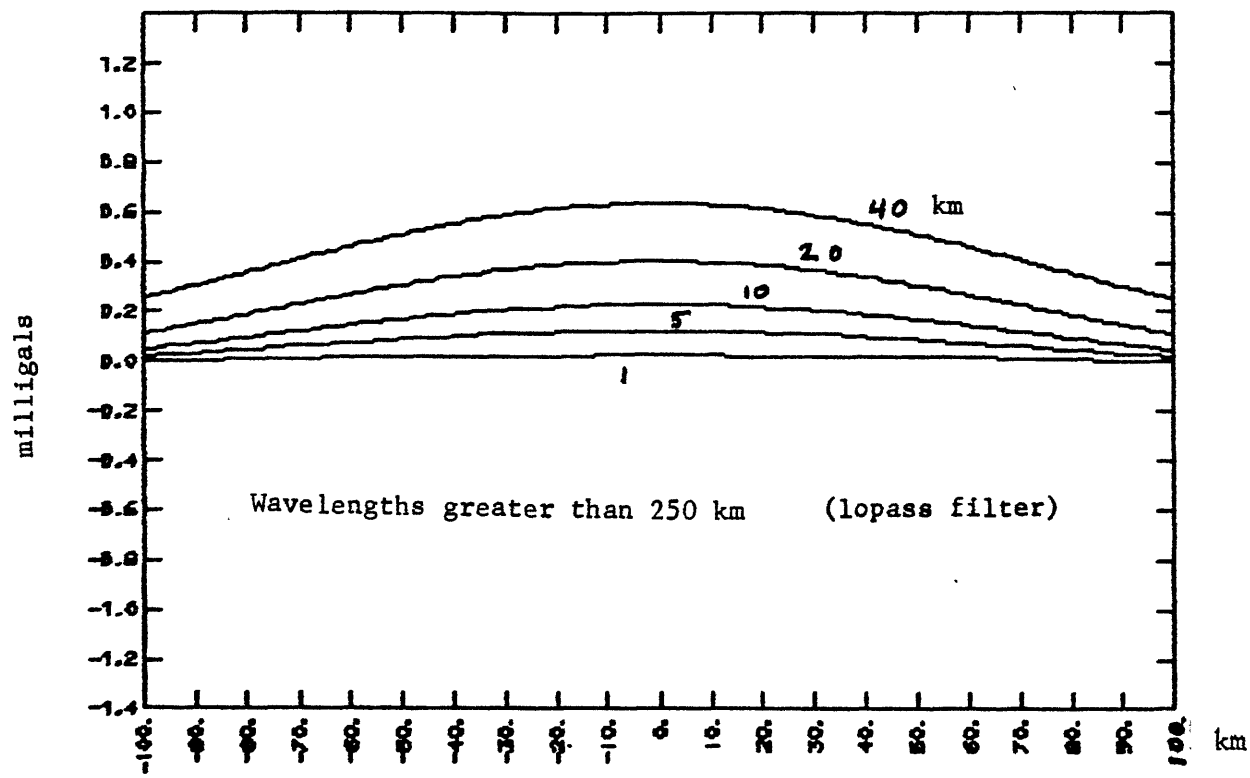

Figure 2d. Long wavelength component (greater than 250 km) for same bodies as in figure 2b.

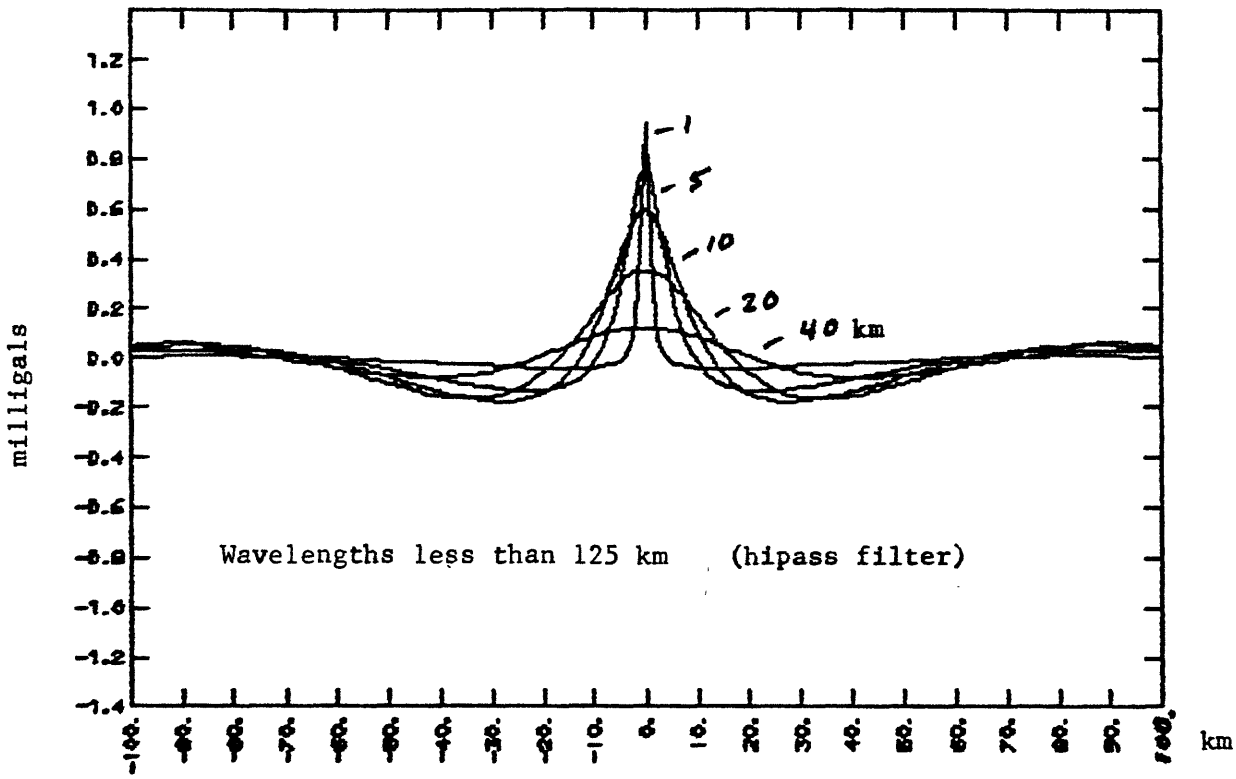

Figure 2e. Short wavelength component (less than 125 km) for same bodies as in figure 2b.

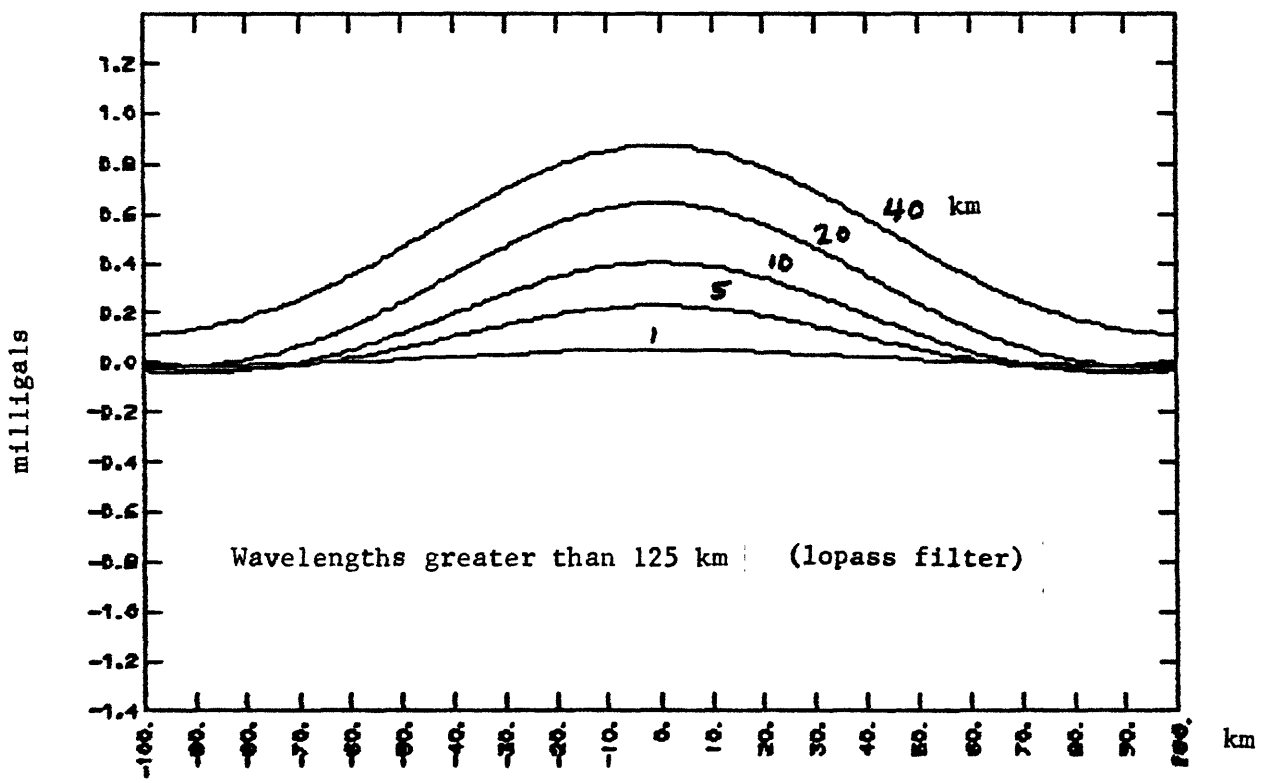

Figure 2f. Long wavelength component (greater than 125 km) for same bodies as in figure 2b.

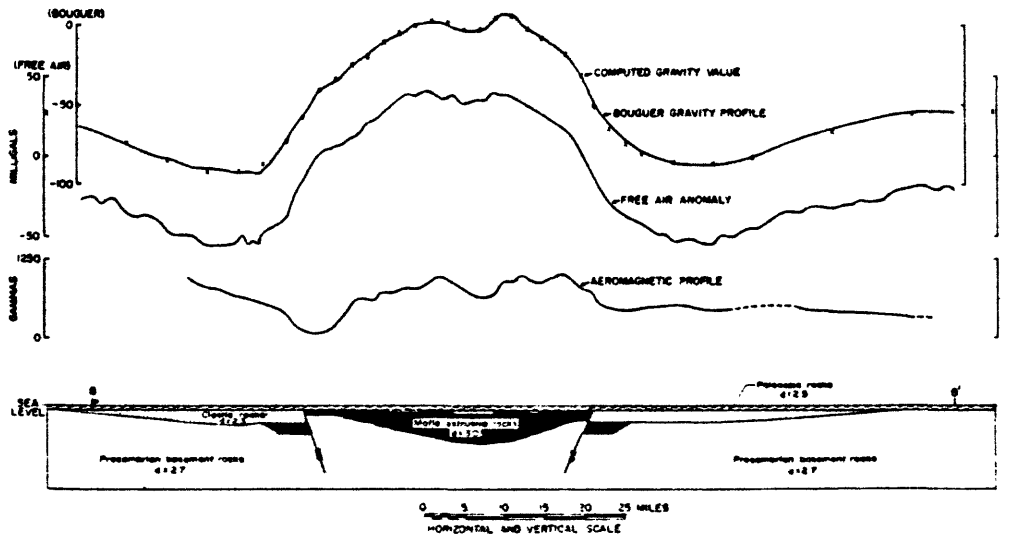

Figure 3a. A profile across the mid-continent gravity high from King and Zietz (1971, Figure 5).

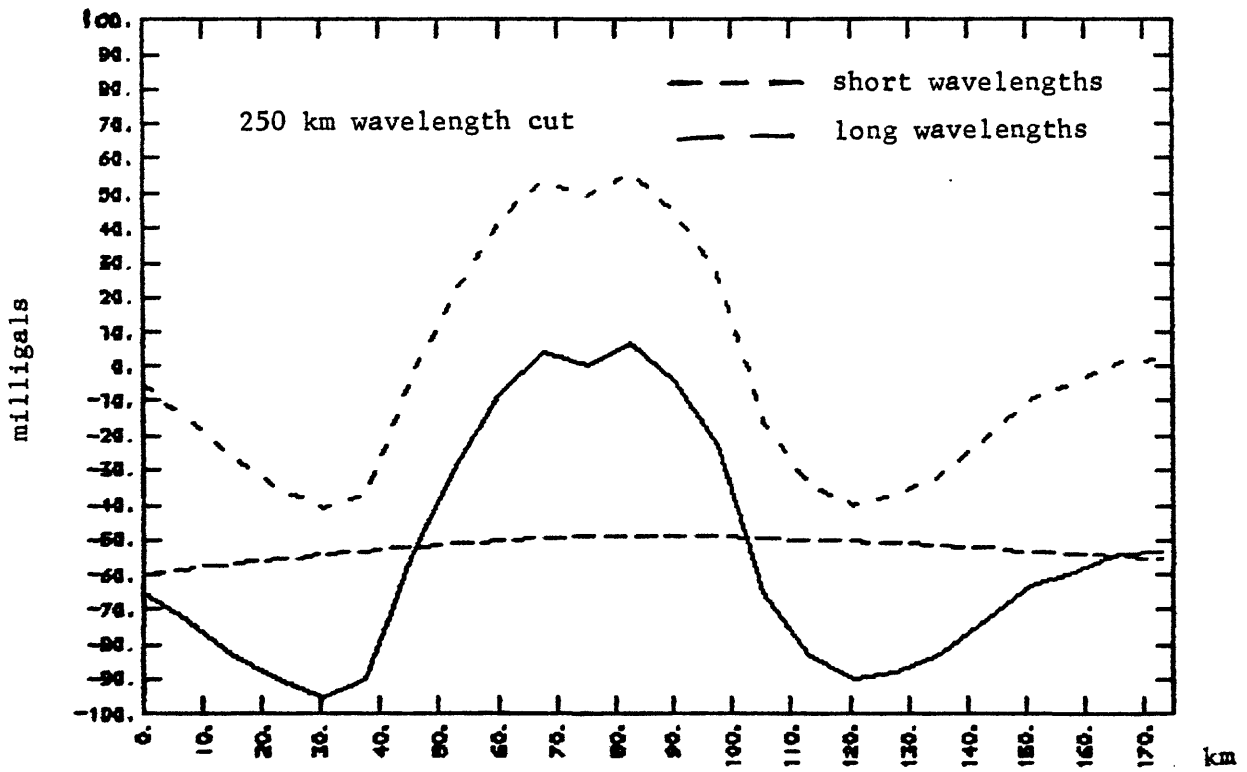

Figure 3b. Solid line is Bouguer gravity profile shown in figure 3a. Short dashes mark component from wavelengths less than 250 km, long dashes component from wavelength greater than 250 km.

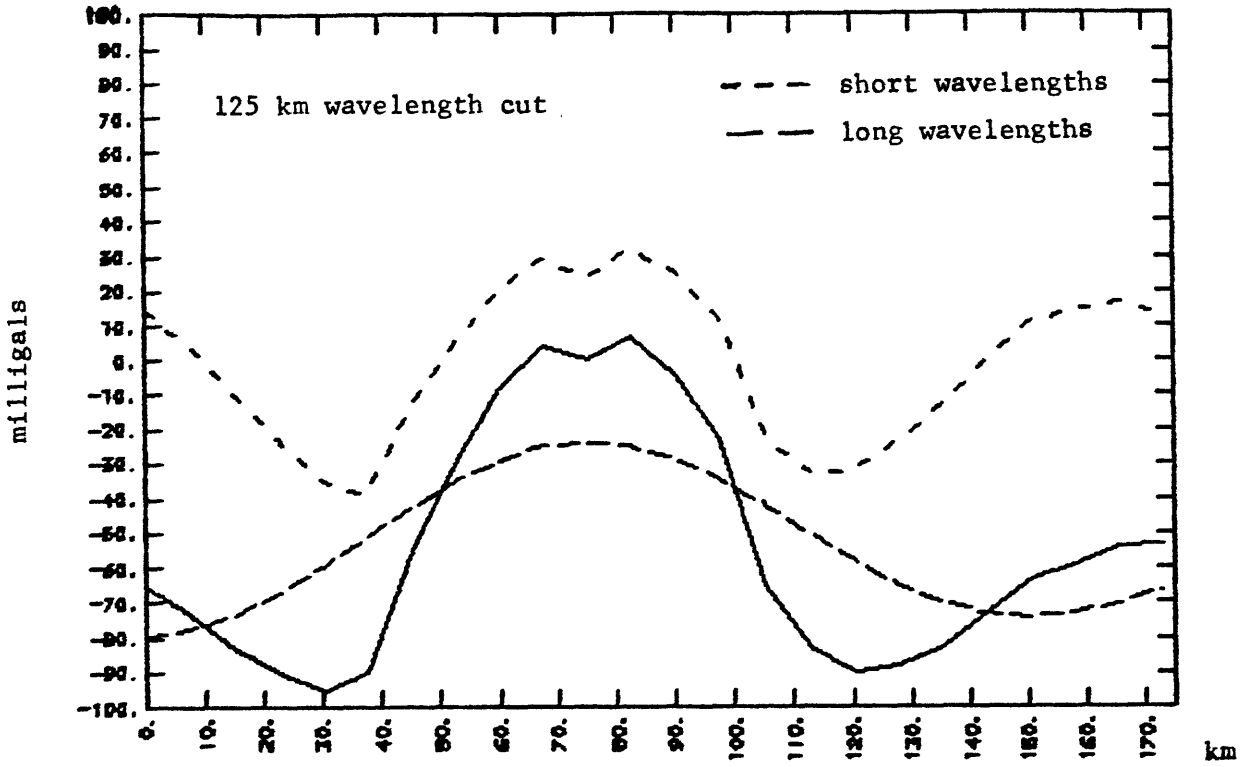

Figure 3c. Same as in figure 3b, but filter cut at 125 km.

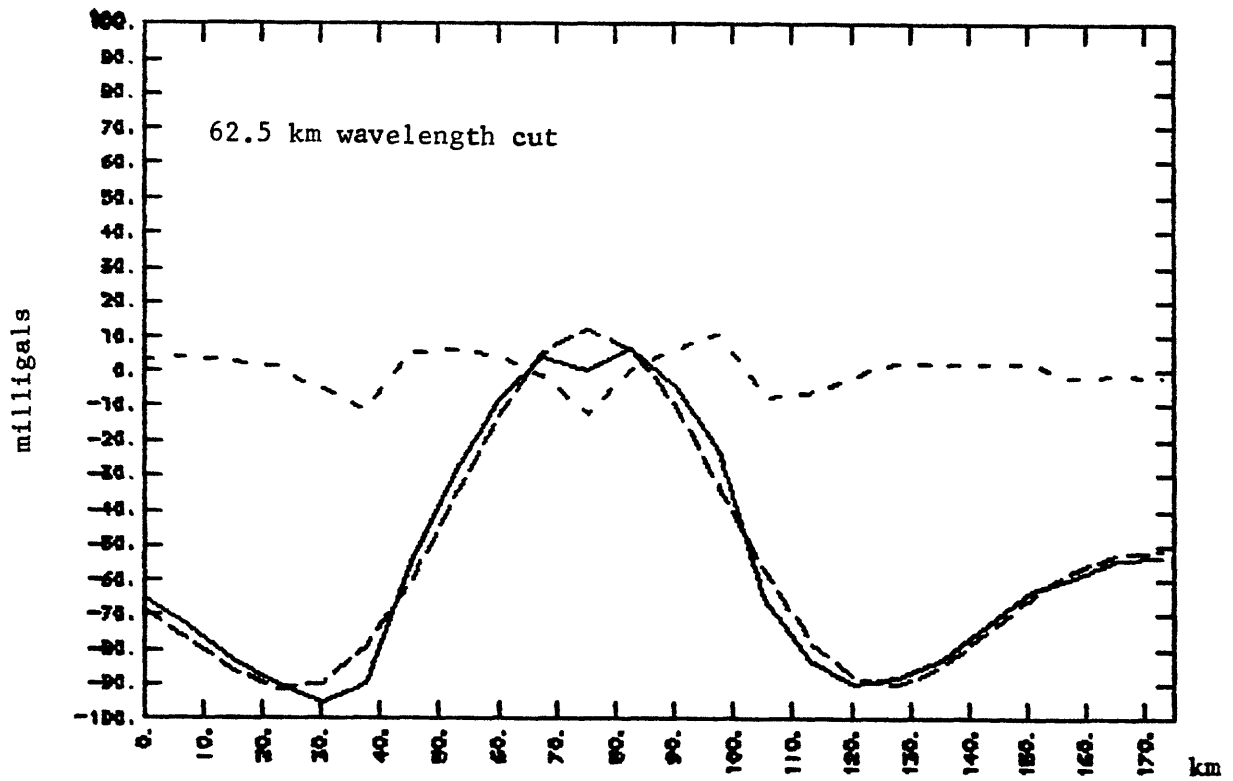

Figure 3d. Same as in figure 3b, but filter cut at 62.5 km.